

The Primordial Inflation Explorer (PIXIE)

Alan Kogut^a, David T. Chuss, Jessie Dotson^b, Dale J. Fixsen^a, Mark Halpern^c, Gary F. Hinshaw^c, Stephan Meyer^d, S. Harvey Moseley^a, Michael D. Seiffert^e, David N. Spergel^f, and Edward J. Wollack^a

^aCode 665, NASA Goddard Space Flight Center, Greenbelt, MD USA 20771;

^bNASA Ames Research Center, Moffett Field, CA, USA 94035;

^cDept. of Physics & Astronomy, University of British Columbia, Vancouver, BC, Canada, V6T 1Z1;

^dDept of Astronomy & Astrophysics, University of Chicago, Chicago, IL, USA;

^eJet Propulsion Laboratory, MS 169-506, Pasadena, CA, USA 91109;

^fDept of Astrophysical Sciences, Princeton University, Princeton, NJ, USA 08544

ABSTRACT

The Primordial Inflation Explorer is an Explorer-class mission to measure the gravity-wave signature of primordial inflation through its distinctive imprint on the linear polarization of the cosmic microwave background. PIXIE uses an innovative optical design to achieve background-limited sensitivity in 400 spectral channels spanning 2.5 decades in frequency from 30 GHz to 6 THz (1 cm to 50 μ m wavelength). Multi-moded non-imaging optics feed a polarizing Fourier Transform Spectrometer to produce a set of interference fringes, proportional to the difference spectrum between orthogonal linear polarizations from the two input beams. The differential design and multiple signal modulations spanning 11 orders of magnitude in time combine to reduce the instrumental signature and confusion from unpolarized sources to negligible levels. PIXIE will map the full sky in Stokes I , Q , and U parameters with angular resolution 2.6° and sensitivity 0.2μ K per 1° square pixel. The principal science goal is the detection and characterization of linear polarization from an inflationary epoch in the early universe, with tensor-to-scalar ratio $r < 10^{-3}$ at 5 standard deviations. We describe the PIXIE instrument and mission architecture needed to detect the signature of an inflationary epoch in the early universe using only 4 semiconductor bolometers.

Keywords: polarimeter, cosmic microwave background, Fourier transform spectrometer, bolometer

1. INTRODUCTION

Linear polarization of the cosmic microwave background (CMB) carries the oldest information in the universe. Quantum fluctuations of the space-time metric (gravity waves) excited only 10^{-35} seconds after the Big Bang impart a distinctive signature to the CMB polarization. Such a signal is expected to exist; the simplest inflation models predict detectable amplitudes in the range 30–100 nK. Detection of the gravity-wave signature of inflation would have profound consequences for cosmology and high-energy physics. Not only would it establish inflation as a physical reality; it would provide a direct, model-independent determination of the relevant energy scale, shedding light on physics at energies 12 orders of magnitude beyond those accessible to direct experimentation in particle accelerators.

CMB polarization results from Thomson scattering of CMB photons by free electrons. A quadrupolar anisotropy in the radiation incident on each electron creates a net linear polarization in the scattered radiation. The required quadrupole can result from either intrinsic fluctuations in the radiation field itself, or the differential redshift as tensor gravity waves propagate through an isotropic medium. The two components can be distinguished by their different angular properties. Density fluctuations are a scalar quantity; their polarization signal must therefore be curl-free. Gravity waves, however, are tensor perturbations whose polarization includes both gradient and curl components. In analogy to electromagnetism, the scalar and curl components are often called “E” and “B”

Send correspondence to: Alan.J.Kogut@nasa.gov; telephone 1 301 286 0853

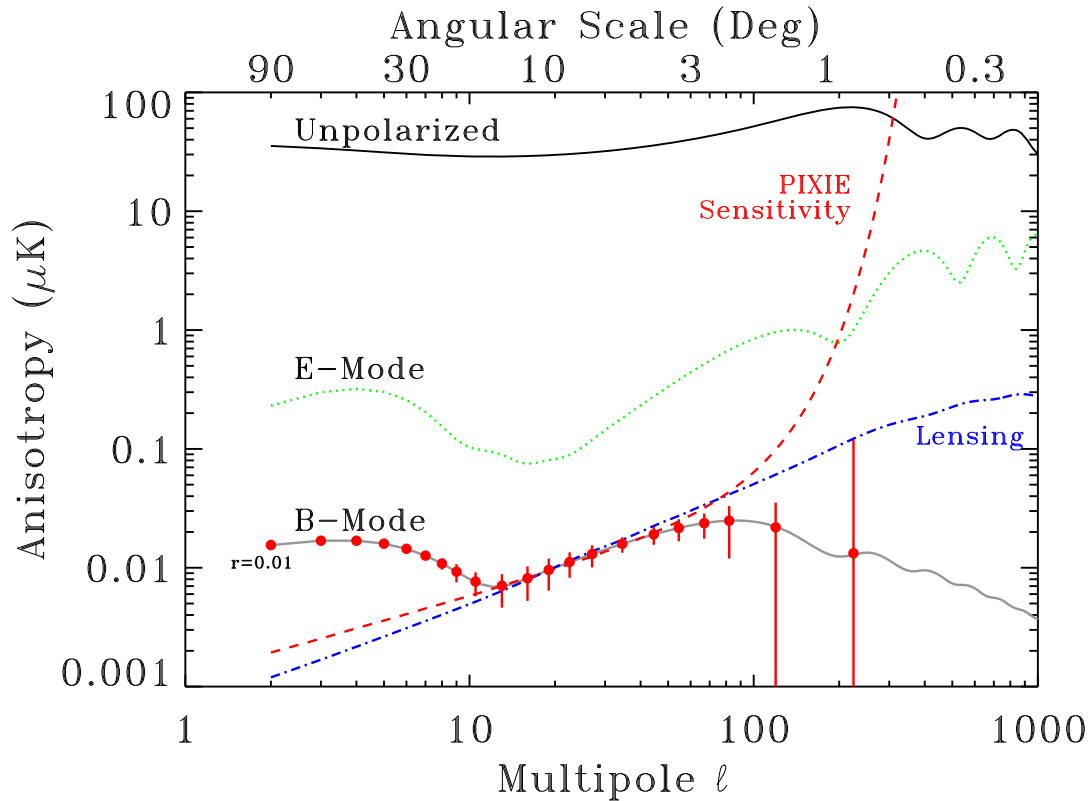


Figure 1. Angular power spectra for unpolarized, E-mode, and B-mode polarization in the cosmic microwave background. The dashed line shows the PIXIE sensitivity to B-mode polarization at each multipole moment $\ell \sim 180^\circ/\theta$. The sensitivity estimate assumes a 4-year mission and includes the effects of foreground subtraction within the cleanest 75% of the sky combining PIXIE data at frequencies $\nu < 600$ GHz. Filled points and error bars show the response within broader ℓ bins to a B-mode power spectrum with amplitude $r = 0.01$. PIXIE will reach the confusion noise from the gravitational lensing of the E-mode signal by cosmic shear along each line of sight (dash-dot), and has the sensitivity and angular response to measure even the minimum predicted B-mode power spectrum at high statistical confidence.

modes. Only gravity waves induce a curl component: detection of a B-mode signal in the CMB polarization field is recognized as a “smoking gun” signature of inflation, testing physics at energies inaccessible through any other means.^{1–8}

Figure 1 shows the amplitude of CMB polarization as a function of angular scale. At the degree angular scales characteristic of the horizon at decoupling, the unpolarized temperature anisotropy is typically $80 \mu\text{K}$. These fluctuations in turn generate E-mode polarization, which at amplitude $\sim 3 \mu\text{K}$ is only a few percent of the temperature fluctuations. The B-mode amplitude from gravity waves is unknown. This amplitude is related directly to the energy scale V_* of inflation,⁹ $V_* = r(0.003 M_{pl})^4$, where $M_{pl} = 1.22 \times 10^{19}$ GeV is the Planck mass and $r = T/S$ is the power ratio of gravity waves to scalar fluctuations. If inflation results from Grand Unified Theory physics (energy $\sim 10^{16}$ GeV), the B-mode amplitude should be in the range 1 to 100 nK. Recent WMAP results suggest likely values 30–100 nK, toward the upper range of GUT inflation.¹⁰ Signals at this amplitude could be detected by a dedicated polarimeter, providing a direct, model-independent measurement of the energy scale of inflation.

Detecting the gravity-wave signature will be difficult. As recognized in multiple reports,^{11–13} there are three fundamental challenges:

- **Sensitivity** The gravity-wave signal is faint compared to the fundamental sensitivity limit imposed by

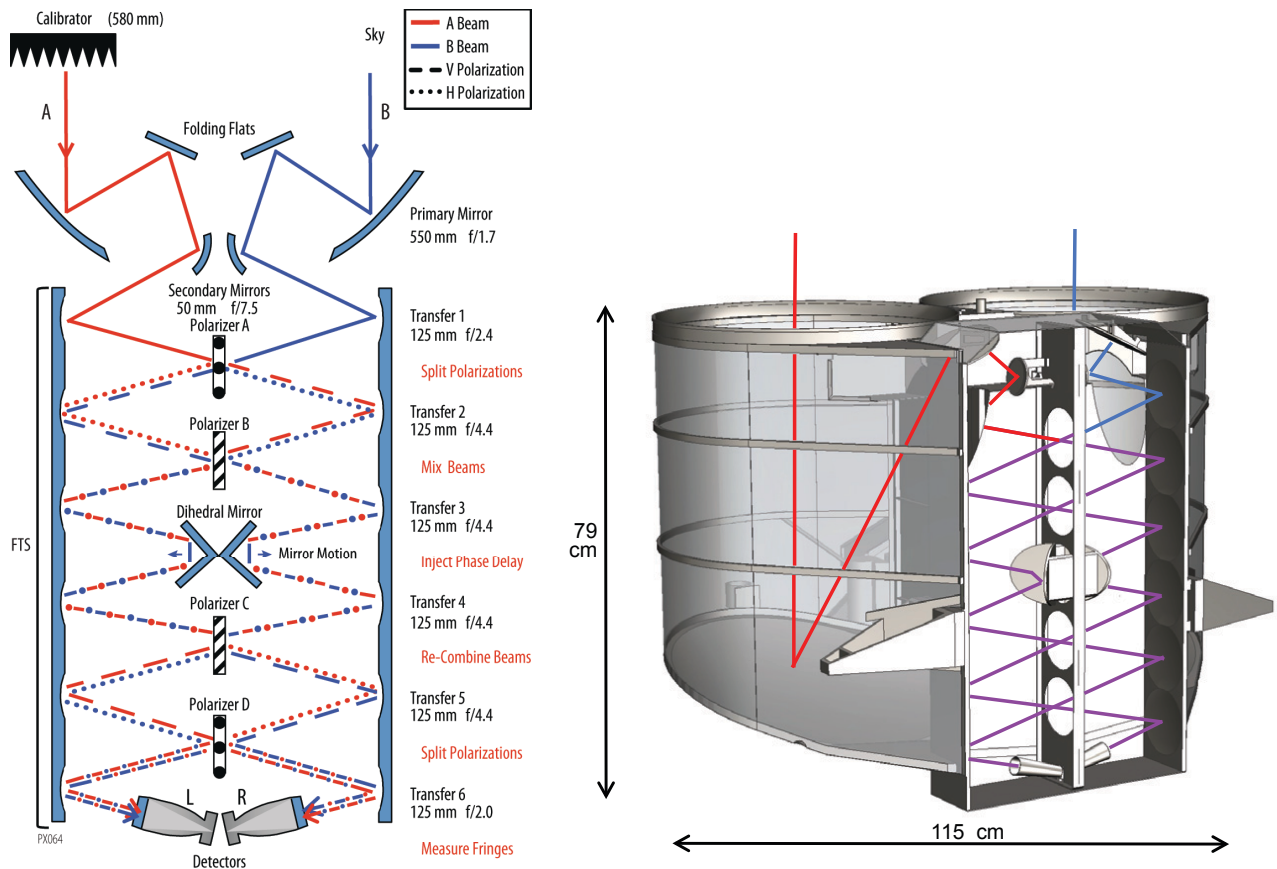


Figure 2. left: Schematic view of the PIXIE optical signal path. As the dihedral mirrors move, the detectors measure a fringe pattern proportional to the Fourier transform of the difference spectrum between orthogonal polarization states from the two input beams (Stokes Q in instrument coordinates). A full-aperture blackbody calibrator can move to block either input beam, or be stowed to allow both beams to view the same patch of sky. Right: Physical layout of PIXIE optics.

photon arrival statistics. Even noiseless detectors suffer from this photon-counting limit; the only solution is to collect more photons.

- **Foregrounds** The gravity-wave signal is faint compared to the polarized Galactic synchrotron and dust foregrounds. Separating CMB from foreground emission based on their different frequency spectra requires multiple frequency channels.
- **Systematic Errors** The gravity-wave signal is faint compared to both the unpolarized CMB anisotropy and the dominant E-mode polarization. Accurate measurement of the B-mode polarization requires strict control of instrumental effects that could alias these brighter signals into a false B-mode detection.

Satisfying the simultaneous requirements of sensitivity, foreground discrimination, and immunity to systematic errors presents a technological challenge. In this paper, we describe an instrument capable of measuring the CMB and diffuse Galactic foregrounds with background-limited sensitivity in over 400 frequency channels using only 4 detectors.

2. INSTRUMENT DESCRIPTION

The Primordial Inflation Explorer (PIXIE) is a concept for an Explorer-class mission to detect and characterize the polarization signal from an inflationary epoch in the early Universe. The proposed instrument combines

Table 1. Optical Parameters

Parameter	Value	Notes
Primary Mirror Diameter	55 cm	Sets beam size on sky
Etendu	4 cm ² sr	2.7 times larger than FIRAS
Beam Diameter	2°6 tophat	Equivalent 1°6 Gaussian FWHM
Throughput	82%	Excludes detector absorption
Detector Absorption	54%	Reflective backshort
Mirror Stroke	±2.6 mm peak-peak	Phase delay ±10 mm
Spectral Resolution	15 GHz	Set by longest mirror stroke
Highest Effective Frequency	6 THz	Spacing in polarizing grids
Detector NEP	0.7×10^{-16} W Hz ⁻¹	Background limit
System NEP	2.7×10^{-16} W Hz ⁻¹	

multi-moded optics with a Fourier Transform Spectrometer to provide breakthrough sensitivity for CMB polarimetry using only four semiconductor detectors. The design addresses each of the principal challenges for CMB polarimetry. A multi-moded “light bucket” provides nK sensitivity using only four detectors. A polarizing Fourier Transform Spectrometer (FTS) synthesizes 400 channels across 2.5 decades in frequency to provide unparalleled separation of CMB from Galactic foregrounds. PIXIE’s highly symmetric design enables operation as a nulling polarimeter to provide the necessary control of instrumental effects.

Figure 2 shows the instrument concept. Two off-axis primary mirrors 550 mm in diameter produce twin beams co-aligned with the spacecraft spin axis. A folding flat and 50 mm secondary mirror route the beams to the FTS. A set of six transfer mirror pairs, each imaging the previous mirror to the following one, shuttles the radiation through a series of polarizing wire grids. Polarizer A transmits vertical polarization and reflects horizontal polarization, separating each beam into orthogonal polarization states. A second polarizer (B) with wires oriented 45° relative to grid A mixes the polarization states. A Mirror Transport Mechanism (MTM) moves back-to-back dihedral mirrors to inject an optical phase delay. The phase-delayed beams re-combine (interfere) at Polarizer C. Polarizer D (oriented the same as A) splits the beams again and routes them to two multi-moded concentrator feed horns. Each concentrator is square to preserve linear polarization and contains a pair of identical bolometers, each sensitive to a single linear polarization but mounted at 90° to each other to measure orthogonal polarization states. To control stray light, all internal surfaces except the active optical elements are coated with a microwave absorber,¹⁴ forming a blackbody cavity isothermal with the sky.

Table 1 summarizes the instrument optics. Cryogenic pupil stops at the primary mirror and field stops at the transfer mirrors limit the etendu to 4 cm² sr to produce a circular tophat beam with diameter 2°6*. Throughput from the entrance aperture to the detector is 82%, evenly split among geometric loss, diffractive loss, and absorption on the wire grids. A low-pass filter on each folding flat blocks zodiacal light. The optics, including the square concentrator, preserve polarization: orthogonal polarization states at the detector remain orthogonal within 3° when projected to the sky.

Each of the four detectors measures an interference fringe pattern between orthogonal linear polarizations from the two input beams. Let $\vec{E} = E_x \hat{x} + E_y \hat{y}$ represent the electric field incident from the sky. The power at the detectors as a function of the mirror position z may be written

$$\begin{aligned}
 P_{Lx} &= \frac{1}{2} \int (E_{Ax}^2 + E_{By}^2) + (E_{Ax}^2 - E_{By}^2) \cos(4z\omega/c) d\omega \\
 P_{Ly} &= \frac{1}{2} \int (E_{Ay}^2 + E_{Bx}^2) + (E_{Ay}^2 - E_{Bx}^2) \cos(4z\omega/c) d\omega \\
 P_{Rx} &= \frac{1}{2} \int (E_{Ay}^2 + E_{Bx}^2) + (E_{Bx}^2 - E_{Ay}^2) \cos(4z\omega/c) d\omega
 \end{aligned}$$

*The angular smoothing from the tophat beam (window function in ℓ) may be approximated by a 1°6 Gaussian full width at half maximum.

$$P_{Ry} = \frac{1}{2} \int (E_{Ax}^2 + E_{By}^2) + (E_{By}^2 - E_{Ax}^2) \cos(4z\omega/c) d\omega, \quad (1)$$

(Appendix A), where ω is the angular frequency of incident radiation, L and R refer to the detectors in the left and right concentrators, and A and B refer to the two input beams

The term modulated by the mirror scan is proportional to the Fourier transform of the frequency spectrum for Stokes Q linear polarization in instrument-fixed coordinates. Rotation of the instrument about the beam axis interchanges \hat{x} and \hat{y} on the detectors. The sky signal (after the Fourier transform) then becomes

$$\begin{aligned} S(\nu)_{Lx} &= \frac{1}{4} [I(\nu)_A - I(\nu)_B + Q(\nu)_{\text{sky}} \cos 2\gamma + U(\nu)_{\text{sky}} \sin 2\gamma] \\ S(\nu)_{Ly} &= \frac{1}{4} [I(\nu)_A - I(\nu)_B - Q(\nu)_{\text{sky}} \cos 2\gamma - U(\nu)_{\text{sky}} \sin 2\gamma] \\ S(\nu)_{Rx} &= \frac{1}{4} [I(\nu)_B - I(\nu)_A + Q(\nu)_{\text{sky}} \cos 2\gamma + U(\nu)_{\text{sky}} \sin 2\gamma] \\ S(\nu)_{Ry} &= \frac{1}{4} [I(\nu)_B - I(\nu)_A - Q(\nu)_{\text{sky}} \cos 2\gamma - U(\nu)_{\text{sky}} \sin 2\gamma], \end{aligned} \quad (2)$$

where $I = \langle E_x^2 + E_y^2 \rangle$, $Q = \langle E_x^2 - E_y^2 \rangle$, and $U = 2\text{Re}\langle E_x E_y \rangle$ are the Stokes polarization parameters, γ is the spin angle, and $S(\nu)$ denotes the synthesized frequency spectrum with bins ν set by the fringe sampling.

The fringe pattern measured at each detector samples the Fourier transform of the frequency spectrum of the difference between one linear polarization from the A-side beam and the orthogonal linear polarization from the B-side beam (Eq. 1). The frequency bins in the synthesized spectra $S(\nu)$ are set by the mirror throw and detector sampling,

$$S_\nu = \sum_{k=0}^{N_s-1} S_i \exp(2\pi i \nu k / N_s) \quad (3)$$

where S_i is a time-ordered sample and ν denotes frequency. As the mirror moves, we obtain N_s detector samples over an optical path length $\pm \Delta L$. The Fourier transform of the sampled fringe pattern returns frequencies $n \times c/(2\Delta L)$ where $n = 0, 1, 2, \dots, N_s/2$. The path length (optical stroke) thus determines the width of the frequency bins in the synthesized spectra, while the number of detector samples within each optical stroke determines the number of frequency bins and thus the highest sampled frequency. With $N_s = 1024$ and $\Delta L = 1$ cm, we obtain 512 synthesized frequency bins of width 15 GHz each. The corresponding physical mirror movement $\Delta z = \Delta L/[4\cos(\alpha)\cos(\delta/2)] = \pm 2.58$ mm accounts for the folded optics as well as the off-axis optical path ($\alpha = 15^\circ$) and beam divergence ($\delta = 6.5^\circ$).

PIXIE operates as a nulling polarimeter: when both beams view the sky, the instrument nulls all unpolarized emission so that the fringe pattern responds only to the sky polarization. The resulting null operation greatly reduces sensitivity to systematic errors from unpolarized sources. Normally the instrument collects light from both co-aligned telescopes. A full-aperture blackbody calibrator can move to block either beam, replacing the sky signal in that beam with an absolute reference source, or be stowed to allow both beams to view the same sky patch. The calibrator temperature is maintained near 2.725 K and is changed ± 5 mK every other orbit to provide small departures from null as an absolute reference signal. When the calibrator blocks either beam, the fringe pattern encodes information on both the temperature distribution on the sky (Stokes I) as well as the linear polarization. Interleaving observations with and without the calibrator allows straightforward transfer of the absolute calibration scale to linear polarization, while providing a valuable cross-check of the polarization solutions obtained in each mode.

Figure 3 shows the observatory and mission concept. The two parallel beams point along the spacecraft spin axis, which is maintained perpendicular to the Sun line and nearly anti-nadir to minimize signals from the Sun or the Earth. An external blackbody calibrator moves to cover either beam and can be stowed to leave both beams open to the sky. The calibrator, beam-forming optics, beam splitters, and interferometer are maintained at 2.725 K to remain in thermal equilibrium with the sky. Each semiconductor bolometer is cooled to base temperature 0.1 K using an adiabatic demagnetization refrigerator. The observatory operates from a 660 km polar sun-synchronous

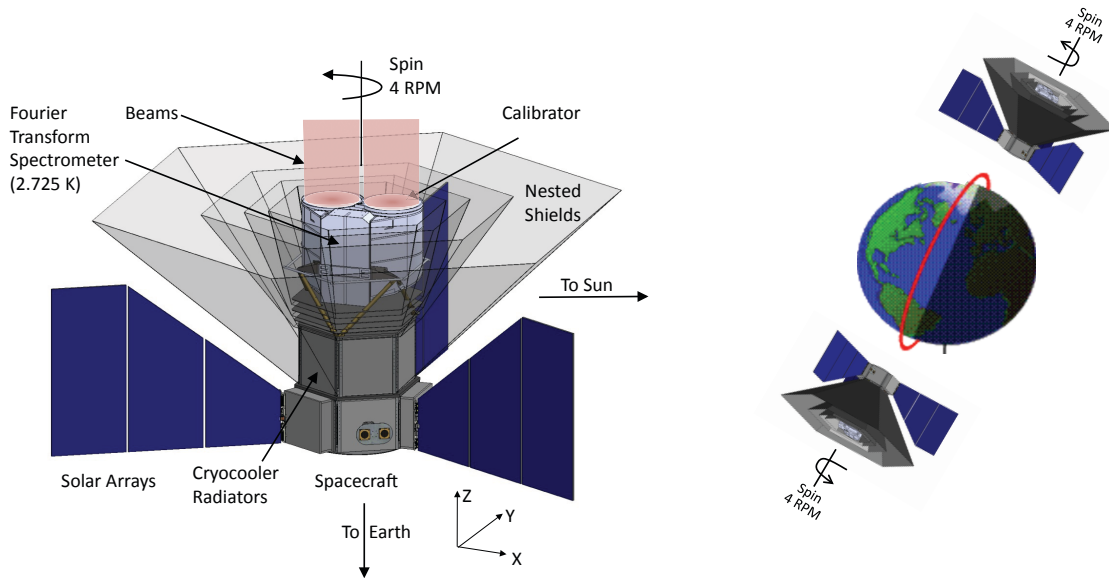


Figure 3. PIXIE observatory and mission concept. The instrument is maintained at 2.725 K and is surrounded by shields to block radiation from the Sun or Earth. It observes from a 660 km polar sun-synchronous terminator orbit. The rapid spin and interferometer stroke efficiently separate Stokes I, Q, and U parameters independently within each pixel to provide a nearly diagonal covariance matrix.

orbit with 6 AM or 6 PM ascending node to allow an unobstructed view to deep space while avoiding emission from the Sun or Earth. The instrument thus observes a great circle each orbit, while the orbit precession of 1° per day achieves full sky coverage in each 6-month observing period. PIXIE is technologically mature and could launch as early as 2017.

3. INSTRUMENT PERFORMANCE

3.1 Sensitivity

The noise equivalent power (NEP) of photon noise in a single linear polarization is given by

$$\text{NEP}_{\text{photon}}^2 = \frac{2A\Omega}{c^2} \frac{(kT)^5}{h^3} \int \alpha \epsilon f \frac{x^4}{e^x - 1} \left(1 + \frac{\alpha \epsilon f}{e^x - 1} \right) dx, \quad (4)$$

where $x = h\nu/kT$, ν is the observing frequency, A is the detector area, Ω is the detector solid angle, α is detector absorptivity, T is the physical temperature of the source, ϵ is the emissivity of the source, and f is the power transmission through the optics.¹⁵ For a fixed integration time τ the detected noise is simply

$$\delta P = \frac{\text{NEP}}{\sqrt{\tau/2}} \quad (5)$$

where the factor of 2 accounts for the conversion between the frequency and time domains. The noise at the detector may in turn be referred to the specific intensity on the sky,

$$\delta I_\nu = \frac{\delta P}{A\Omega \Delta\nu (\alpha \epsilon f)} \quad (6)$$

where $\Delta\nu$ is the observing bandwidth.

PIXIE combines a large collecting area with non-imaging optics to maximize the number of photons while minimizing the detector count. The light-gathering ability of an instrument is specified by its etendu $A\Omega$. Increasing the etendu for a single detector increases the photon noise, $\text{NEP} \propto (A\Omega)^{1/2}$, thereby decreasing the relative contribution of the intrinsic detector (phonon) noise. But since the signal increases linearly with etendu, the signal-to-noise ratio *improves* as $(A\Omega)^{1/2}$. Increasing the etendu relaxes detector noise requirements while simultaneously improving the overall system sensitivity to sky signals.

The multi-moded PIXIE optics provide sensitivity comparable to kilo-pixel focal plane arrays while requiring only 4 semiconductor bolometers. For diffraction-limited single-mode optics, the etendu and wavelength are related as $A\Omega = \lambda^2$ so that the beam size scales with the observing wavelength. For multi-moded optics, however, the beam size is fixed and the number of modes N scales as $N = A\Omega/\lambda^2$. Multi-moded optics thus allow a considerable increase in sensitivity compared to single-moded designs of comparable size. The improvement is large enough to allow precision measurement of the gravity-wave signature in polarization using a handful of detectors. Over just the frequency range 30–600 GHz where the CMB is brightest, each PIXIE detector measures 22,000 independent modes of the electric field.

With the calibrator deployed over either aperture, the instrument measures both polarized and unpolarized emission (Stokes I , Q , and U). With both beams open to the sky, the instrument is insensitive to unpolarized emission but has twice the sensitivity to polarized signals[†]. Averaging over the four detectors, the combined instrument sensitivity to either unpolarized or polarized emission within each synthesized frequency bin is

$$\begin{aligned}\delta I_\nu^I &= 2.4 \times 10^{-22} \text{ W m}^{-2} \text{ sr}^{-1} \text{ Hz}^{-1} \\ \delta I_\nu^{QU} &= 3.4 \times 10^{-22} \text{ W m}^{-2} \text{ sr}^{-1} \text{ Hz}^{-1}\end{aligned}\tag{7}$$

for a one-second integration with the calibrator deployed over either aperture, and

$$\delta I_\nu^{QU} = 0.5 \times 10^{-22} \text{ W m}^{-2} \text{ sr}^{-1} \text{ Hz}^{-1}\tag{8}$$

when the calibrator is stowed.¹⁶ PIXIE will spend approximately 30% of the observing time with the calibrator deployed and 60% with the calibrator stowed. The remaining 10% includes both high-temperature calibration of the Galactic dust signal and lost observing time.

Eqs 7 and 8 give the specific intensity within each synthesized frequency bin. The wire grid polarizers become inefficient in reflection at wavelengths $\lambda < 60 \mu\text{m}$ defined by the $30 \mu\text{m}$ wire spacing, limiting the effective frequency coverage to 400 bins from 30 GHz to 6 THz (Fig 4). For continuum sources like the CMB we may integrate over multiple bins to further improve sensitivity. Table 2 shows the resulting sensitivity to a CMB source. A 2-year mission achieves rms sensitivity 200 nK within each $1^\circ \times 1^\circ$ pixel, falling to 70 nK with 4 years of observations.¹⁶

Cosmological foregrounds present a natural sensitivity limit. Primordial density perturbations source E-mode polarization. Gravitational lensing from the mass distribution along each line of sight creates a shear that distorts the orientation of the primordial polarization field, analogous to the shear in galaxy orientations observed along the line of sight toward distant massive clusters. By perturbing the polarization orientation, gravitational lensing mixes the E and B modes and transforms a small fraction of the dominant E-mode polarization into a B-mode. On angular scales $\theta > 0.5$, the lensed B-mode signal is well approximated by a random white noise field on the sky (Fig 1). This sky noise is present along every line of sight and adds in quadrature with the instrument noise. PIXIE will reach this cosmological “noise floor” beyond which little additional gain can be realized.

The PIXIE sensitivity allows robust detection and characterization of the inflationary B-mode signal. Averaged over the cleanest 75% of the sky, PIXIE will detect the gravity-wave signal $r < 10^{-3}$ at 5 standard deviations, two orders of magnitude more sensitive than Planck and a factor of ten below the predicted signal for GUT-scale inflation. The resulting sensitivity allows characterization of the B-mode angular power spectrum in ~ 20 bins at multipoles $\ell < 100$ limited by the 2.6° diameter beam (Figure 1).

[†]Replacing the blackbody calibrator emission with sky emission in one beam leaves the noise nearly unchanged but doubles the sky signal incident on the FTS.

Table 2. Observatory CMB Sensitivity

Observing Mode	NET ($\mu\text{K s}^{1/2}$)	NEQ ($\mu\text{K s}^{1/2}$)
Calibrator Deployed	13.6	19.2
Calibrator Stowed	—	5.6

3.2 Foregrounds

On the large angular scales of interest to PIXIE, foregrounds are dominated by polarized emission from the Milky Way's interstellar medium.^{12,17} Polarized emission within the Galaxy is dominated by two main sources. Synchrotron radiation from cosmic ray electrons accelerated in the Galactic magnetic field approximates a power-law spectrum

$$I(\nu)_{\text{synch}} \propto \nu^{\beta_s} \quad (9)$$

with $\beta_s \sim -0.7$. Thermal emission from dust grains follows a greybody spectrum,

$$I(\nu)_{\text{dust}} \propto B_\nu(T_{\text{dust}})\nu^{\beta_d} \quad (10)$$

with $\beta_d \sim 1.7$. CMB emission follows a Planck spectrum, with power-law spectral index $\beta = 2$ in the low-frequency Rayleigh-Jeans portion and an exponential cutoff on the Wien side of the blackbody spectrum (Fig 4).

CMB emission can be distinguished from Galactic foregrounds based on their different frequency spectra. The number of independent frequency channels must equal or exceed the number of free parameters to be derived from a multi-frequency fit. A conservative approach requires at least ten frequency channels at the millimeter wavelengths where the CMB is brightest: three parameters (amplitude, spectral index, and spectral curvature) for synchrotron emission, three parameters (amplitude, spectral index, and frequency-dependent polarization fraction) for thermal dust emission, two parameters (amplitude and spectral index) for electric dipole emission from a population of rapidly spinning dust grains, one parameter (amplitude) for free-free emission (thermal bremsstrahlung) reflected from diffuse interstellar dust, and one parameter (amplitude) for CMB polarization.

A commonly used technique forms a linear combination of frequency channels,

$$T_{\text{ILC}} = \sum_{\nu} \alpha_{\nu} T_{\nu} , \quad (11)$$

to separate CMB from foreground emission based on the different spectra. If the component spectra are known, the coefficients α_{ν} may be chosen such that a CMB spectrum is recovered with unit response while the foreground signals are canceled.^{18,19} A useful way to express sensitivity is to quote the Foreground Degradation Factor (FDF), the ratio of the noise per pixel in the foreground-reduced map to corresponding noise obtained using straight noise weighting. PIXIE has many more frequency channels than foreground components, allowing efficient foreground suppression without excessive noise penalty. PIXIE achieves FDF=1.02 – the noise penalty for rejecting foregrounds with PIXIE is only 2%. This noise penalty is included in all estimates of CMB sensitivity.

The internal linear combination technique requires knowledge of the foreground spectral indices. PIXIE has 400 effective channels from 30 GHz to 6 THz, allowing independent determination of the spectral indices within each sky pixel. PIXIE primarily observes at frequencies above 100 GHz where the dominant foreground is dust. Simulations using realistic polarized foregrounds^{20,21} and instrument noise successfully recover the long-wavelength dust index from the input maps to 0.06% precision, corresponding to ± 0.001 uncertainty in the dust spectral index. The resulting error in the recovered CMB component is below 1 nK.

The broad frequency range of the PIXIE data provides rich ancillary science in addition to the primary goal of inflationary science. Thomson scattering of CMB photons from free electrons at the epoch of reionization sources E mode polarization on large angular scales. The same scattering necessarily distorts the unpolarized CMB away from a blackbody. PIXIE will observe both the E-mode polarization and unpolarized spectral distortion. The

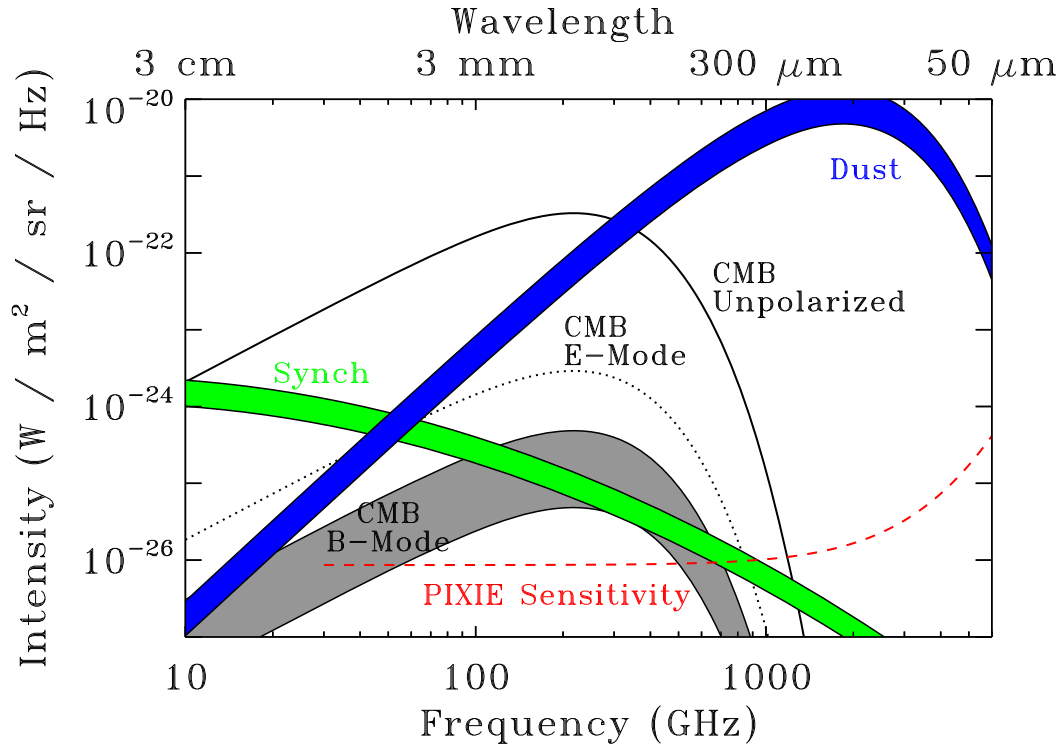


Figure 4. RMS anisotropy for the CMB and polarized foregrounds. The dashed line shows the rms noise within each synthesized frequency channel, averaged over the high-latitude sky. The grey band shows the range of amplitudes $0.01 < r < 0.1$ for the primordial gravity-wave signal. The width of the dust and synchrotron bands reflects rms foreground variation along high-latitude lines of sight. PIXIE combines multi-moded optics with a Fourier Transform Spectrometer to achieve high sensitivity in 400 spectral channels spanning 2.5 decades in frequency.

combination can be used to fix not only the optical depth, but also the gas temperature, and hence provide information on the ionization mechanism at redshift $z \sim 10$. PIXIE data in the far-infrared will characterize the monopole, dipole, and higher-order power spectrum of the far-IR background to test the matter distribution at redshift $z \sim 3$. PIXIE will measure line emission from the interstellar medium, including the prominent CII (158 μm), NII (205 μm), and OI (63 μm) lines as well as the CO series.

3.3 Systematic Errors

Reliable detection of the primordial gravity-wave signal requires rigorous control of systematic errors. PIXIE's highly symmetric design provides multiple levels of rejection for potential instrumental effects. Each detector measures the difference between the \hat{x} polarization from one beam and the \hat{y} polarization from the other beam. The four detectors thus sample different combinations of \hat{x} vs \hat{y} polarization from the A vs B beams in the left vs right optics (Eq. 1). Common-mode instrumental effects cancel in the appropriate sum or difference of selected detector pairs.¹⁶

The primordial B-mode signal is faint compared to the photon noise within a single interferogram. PIXIE's design mitigates the effects of low-frequency $1/f$ noise. An AC bias circuit modulates the detector output at 1 kHz to reduce the amplitude of $1/f$ noise from the detector or readout electronics. The Fourier transform acts on short (1 second) stretches of data. Each interferogram is independent: $1/f$ noise or baseline drifts on time scales much longer than 1 second appear as a constant slope or low-order polynomial in the spatial frequency basis of any single interferogram. The Fourier transform of such low-order polynomials affects only the lowest few spectral bins and does not project efficiently onto either the CMB or foreground spectra. $1/f$ noise is thus inefficient at creating striping in the CMB polarization maps.

Table 3. Systematic Error Budget

Effect	Leakage	PIXIE Mitigation						Residual (nK)
		FTS	Spin	Orbit	Xcal	Symmetry	Preflight	
Beam Ellipticity	$E \rightarrow B$		X	X		X	X	2.7
Cross Polarization	$\nabla T^2 \rightarrow B$		X			X	X	1.5
Polarized Sidelobes	$\Delta T \rightarrow B$		X	X		X	X	1.1
Instrumental Polarization	$\Delta T \rightarrow B$		X	X	X	X	X	< 0.1
Polarization Angle	$E \rightarrow B$			X		X	X	0.7
Pointing Offset	$\Delta T \rightarrow B$		X	X	X	X	X	0.7
Relative Gain	$\Delta T \rightarrow B$	X	X		X	X		< 0.1
Scan-Synch Gain	$T \rightarrow B$	X	X		X	X		< 0.1
Scan-Synch Offset	$T \rightarrow B$	X	X		X	X	X	< 0.1

Statistical characterization of the B-mode signal requires accurate knowledge of the noise properties of the polarization spectral maps. The spatial symmetry of the fringe pattern about zero path length forces the sky signal entirely into the real part of the Fourier transform. The imaginary component of the Fourier transform provides an independent realization of the instrument noise, including systematics and any $1/f$ component, sampled at the same time and through the same optics as the noise in the sky spectra. The imaginary spectral maps may be analyzed identically to the real spectral maps (including multipole power spectra) as blind tests of systematics, with identical noise amplitude as the analyzed signal maps.

A number of authors have examined systematic errors for CMB polarimetry.^{11,22–30} These systematic errors may be grouped into several broad categories. Scan-synchronous effects, which accumulate coherently through multiple observations, are of particular concern for CMB polarimetry. Amplitude modulation of the observed fringe pattern by the spacecraft spin efficiently rejects simple scan-synchronous pickup or offset variation. Scan-synchronous modulation of the instrument responsivity (gain drift) is more serious. Variation in responsivity at twice the spin period will modulate the dominant unpolarized signal to mimic a polarized source. PIXIE’s null design mitigates such a systematic error. With the calibrator stowed, the instrument responds only to polarized sky emission, removing the source term for gain modulation. Gain drifts only affect data when the calibrator is deployed. The calibrator is maintained within 10 mK of the sky temperature to allow operation near null. The residual systematic error signal is linear in the sky-calibrator temperature difference, while true sky signals are independent of the calibrator. Calibration data taken at different calibrator temperature allows identification and removal of scan-synchronous gain drifts. Residual modulation (e.g. from instrument asymmetries) can be rejected by comparing the signal from the 4 independent detectors. Gain drifts are predominantly common mode and produce identical signals on all 4 detectors,. True sky signals have opposite sign for specific detector pairs, allowing separation from common-mode signals.

Beam effects modulate the sky signal and can produce systematic errors. For example, instrument rotation of an elliptical beam pattern over an unpolarized sky creates a spurious “polarization” response at twice the spin frequency as the elliptical beam beats against the quadrupolar component of the local anisotropy. Since beam effects directly modulate the true sky signal, they can not be removed simply by altering the scan strategy and are sometimes referred to as “irreducible” systematic errors. The effect depends on anisotropy on angular scales smaller than the instrument beam and is thus of particular concern for an instrument like PIXIE whose $2^\circ 6'$ beam diameter is larger than the degree angular scale of unpolarized CMB anisotropy.

PIXIE’s differential design mitigates beam-related systematic errors. With the calibrator stowed, the unpolarized signal cancels to leading order, leaving only the differential ellipticity between the A- and B-side beams as a source of potential error. Regardless of calibrator position, polarized and unpolarized signals produce a different sign on each of the four detectors (Eq. 2), allowing unambiguous separation and rejection of beam effects.

A non-zero cross-polar beam response creates systematic errors by mixing the Stokes Q and U parameters, thereby aliasing the dominant E-mode polarization into a spurious B-mode pattern. The dominant cause is the quadrupolar component of the cross-polar beam pattern[‡]. PIXIE’s non-imaging optics produce a tophat

[‡]A cross-polar response that is uniform across the beam affects the amplitude of the response to a polarized sky signal

beam with nearly uniform polarization response, mitigating this effect. As with other beam-related effects, true polarized sky signals enter each detector at a specific relative phase in spin angle and can be identified by the appropriate detector-pair difference.

Table 3 lists the major sources of systematic error and their estimated effect on the PIXIE polarization results. Systematic errors are small compared to the photon noise.

APPENDIX A. OPTICAL SIGNAL PATH

PIXIE is fully symmetric about the plane bisecting the transfer mirrors (Figure 2). Consider a plane wave incident on the instrument A-side primary mirror,

$$\vec{E}_0 = E_x e^{i(kz - \omega t)} \hat{x} + E_y e^{i(kz - \omega t)} \hat{y} \quad (12)$$

where \hat{x} is in the plane of the diagram, \hat{y} is normal to the page, and \hat{z} is along the direction of propagation. For clarity, we will ignore the term $i(kz - \omega t)$ since it is common to all expressions, and denote the amplitude of the field in the \hat{x} and \hat{y} directions as

$$\vec{E}_0 = A\hat{x} + B\hat{y} \quad (13)$$

where $A = E_x$ and $B = E_y$. Reflection from a mirror reverses the direction of propagation and flips the sign of the electric field. Reflections from the primary, folding, and secondary mirrors flip the sign three times and route the beam to the FTS. Reflection from the first transfer mirror flips the sign a fourth time. The field after reflection from the first transfer mirror is thus

$$\vec{E}_1 = \vec{E}_0 = A\hat{x} + B\hat{y} \quad (14)$$

The first polarizing grid transmits the \hat{x} polarization while reflecting \hat{y} . The second left-side transfer mirror collects the beam reflected from the polarizing grid (with a minus sign for the reflection), while the right-side transfer mirror collects the transmitted beam. After reflecting off the second transfer mirror (which induces another sign flip), the fields are

$$\vec{E}_{L2} = B\hat{y} \quad \vec{E}_{R2} = -A\hat{x} \quad (15)$$

where subscripts L and R refer to the left and right sides of the instrument, respectively. The beams then encounter the second polarizing grid, oriented such that from the point of view of the radiation the wires are at 45° from the plane of polarization. Half of each beam is transmitted and half is reflected, imposing a new polarization basis on the radiation which we denote \hat{u} and \hat{v} . The relationship between \hat{u}, \hat{v} and \hat{y}, \hat{z} coordinate systems is

$$\begin{aligned} \hat{u} &= (\hat{x} + \hat{y})/\sqrt{2} \\ \hat{v} &= (\hat{x} - \hat{y})/\sqrt{2} \end{aligned} \quad (16)$$

Hence the radiation just before the second polarizer can be described as

$$\begin{aligned} \vec{E}_{L2} &= B(\hat{u} - \hat{v})/\sqrt{2} \\ \vec{E}_{R2} &= -A(\hat{u} + \hat{v})/\sqrt{2} \end{aligned} \quad (17)$$

The wires of the second polarizer are aligned with the \hat{u} vector so that the E fields in the \hat{u} direction are reflected (with a minus sign) while those in the \hat{v} direction are transmitted.

The third transfer mirror on the left side thus collects the reflected (\hat{u}) radiation from \vec{E}_{L2} (with a minus sign) plus the transmitted (\hat{v}) radiation from \vec{E}_{R2} . The third transfer mirror on the right collects transmitted (\hat{v}) radiation from \vec{E}_{L3} plus the reflected (\hat{u}) radiation from \vec{E}_{R3} (with a minus sign). After reflection from the third transfer mirror (which induces another sign flip), the fields become

$$\vec{E}_{L3} = (B\hat{u} + A\hat{v})/\sqrt{2} \quad \vec{E}_{R3} = (-A\hat{u} + B\hat{v})/\sqrt{2}. \quad (18)$$

(polarization efficiency) but does not mix the E and B modes.

In the original coordinate system we may write this as

$$\vec{E}_{L3} = [(A+B)\hat{x} - (A-B)\hat{y}]/2 \quad \vec{E}_{R3} = [-(A-B)\hat{x} - (A+B)\hat{y}]/2. \quad (19)$$

Note that the second polarizing grid mixes the original polarization states – we began with amplitude A oriented along \hat{x} and amplitude B oriented along \hat{y} . From Eq. 19 we now have linear combinations of A and B along each coordinate axis \hat{x} and \hat{y} .

Each beam then reflects from the dihedral mirror assembly. The dihedral mirror treats the two polarization states differently. The \hat{x} polarization reflects from two faces, generating two canceling negative signs, while the \hat{y} polarization reflects from two faces but also changes direction, resulting in a net change of sign. In addition, the different path length of the left beam with respect to the right beam generates an optical phase delay that depends on the position of the dihedral mirror assembly. The path is shortened on one side but lengthened on the other, creating a total phase delay $e^{+2iz\omega/c}$ on one side and $e^{-2iz\omega/c}$ on the other side, where z is the position of the dihedral mirror assembly. The beams then reflect from the fourth transfer mirror. Including the phase delay, the electric fields after the fourth transfer mirror become

$$\begin{aligned} \vec{E}_{L4} &= [-(A+B)\hat{x} - (A-B)\hat{y}]e^{2iz\omega/c}/2 \\ \vec{E}_{R4} &= [(A-B)\hat{x} - (A+B)\hat{y}]e^{-2iz\omega/c}/2, \end{aligned} \quad (20)$$

or in the rotated coordinate system,

$$\begin{aligned} \vec{E}_{L4} &= (-A\hat{u} - B\hat{v})e^{2iz\omega/c}/\sqrt{2} \\ \vec{E}_{R4} &= (-B\hat{u} + A\hat{v})e^{-2iz\omega/c}/\sqrt{2}. \end{aligned} \quad (21)$$

The beams then recombine at the third polarizing grid. The phases are different (in general) and will lead to either constructive or destructive interference. The wires in the third polarizer are oriented identically to the second polarizer. Radiation leaving the fourth transfer mirror on the left side (\vec{E}_{L4}) will thus reflect the \hat{u} component to the fifth transfer mirror on the left side (with a minus sign) while transmitting the \hat{v} component to the fifth transfer mirror on the right side. The fifth transfer mirror induces another sign change. The fields after the fifth transfer mirror are thus

$$\begin{aligned} \vec{E}_{L5} &= (-A\hat{u}e^{2iz\omega/c} - A\hat{v}e^{-2iz\omega/c})/\sqrt{2} \\ \vec{E}_{R5} &= (-B\hat{u}e^{-2iz\omega/c} + B\hat{v}e^{2iz\omega/c})/\sqrt{2}, \end{aligned} \quad (22)$$

or in the original coordinate system

$$\begin{aligned} \vec{E}_{L5} &= [-A(e^{2iz\omega/c} + e^{-2iz\omega/c})\hat{x} - A(e^{2iz\omega/c} - e^{-2iz\omega/c})\hat{y}]/2 \\ \vec{E}_{R5} &= [B(e^{2iz\omega/c} - e^{-2iz\omega/c})\hat{x} - B(e^{2iz\omega/c} + e^{-2iz\omega/c})\hat{y}]/2 \end{aligned} \quad (23)$$

Re-writing the exponentials as sines and cosines, we obtain

$$\begin{aligned} \vec{E}_{L5} &= -A \cos(2z\omega/c) \hat{x} - iA \sin(2z\omega/c) \hat{y} \\ \vec{E}_{R5} &= iB \cos(2z\omega/c) \hat{x} - B \cos(2z\omega/c) \hat{y} \end{aligned} \quad (24)$$

The beams then encounter the fourth polarizing grid. The wires of the fourth grid are oriented the same as the first grid, reflecting the \hat{y} component while transmitting \hat{x} . After a final reflection from the sixth transfer mirror, the beams reach the detectors. The electric fields at the detectors from radiation originally incident from the left-side beam are thus

$$\begin{aligned} \vec{E}_{L6} &= -iB \sin(2z\omega/c) \hat{x} - iA \sin(2z\omega/c) \hat{y} \\ \vec{E}_{R6} &= A \cos(2z\omega/c) \hat{x} - B \cos(2z\omega/c) \hat{y} \end{aligned} \quad (25)$$

PIXIE has 4 detectors, each of which measures a single linear polarization. The detectors are arranged in two pairs. One member of each pair measures the \hat{x} component while the other member measures \hat{y} . The bolometers measure the incident power, which is the square of the electric field:

$$\begin{aligned} P_{Lx} &= B^2 \sin^2(2z\omega/c) = \frac{1}{2} B^2 [1 - \cos(4z\omega/c)] \\ P_{Ly} &= A^2 \sin^2(2z\omega/c) = \frac{1}{2} A^2 [1 - \cos(4z\omega/c)] \\ P_{Rx} &= A^2 \cos^2(2z\omega/c) = \frac{1}{2} A^2 [1 + \cos(4z\omega/c)] \\ P_{Ry} &= B^2 \cos^2(2z\omega/c) = \frac{1}{2} B^2 [1 + \cos(4z\omega/c)] \end{aligned} \quad (26)$$

The derivation thus far has ignored radiation incident from the B-side beam. Since PIXIE is fully symmetric, the derivation for radiation from the B-side beam is identical to radiation from the A-side beam. Using the principle of superposition we can combine the results from both sides and all frequencies to obtain the power incident on the bolometers as a function of the dihedral mirror position z :

$$\begin{aligned} P_{Lx} &= \frac{1}{2} \int (B^2 + C^2) + (C^2 - B^2) \cos(4z\omega/c) d\omega \\ P_{Ly} &= \frac{1}{2} \int (A^2 + D^2) + (D^2 - A^2) \cos(4z\omega/c) d\omega \\ P_{Rx} &= \frac{1}{2} \int (A^2 + D^2) + (A^2 - D^2) \cos(4z\omega/c) d\omega \\ P_{Ry} &= \frac{1}{2} \int (B^2 + C^2) + (B^2 - C^2) \cos(4z\omega/c) d\omega \end{aligned} \quad (27)$$

where we use notation

$$\begin{aligned} A &= E_x^A = \hat{x} \text{ component of incident E field from A - side beam} \\ B &= E_y^A = \hat{y} \text{ component of incident E field from A - side beam} \\ C &= E_x^B = \hat{x} \text{ component of incident E field from B - side beam} \\ D &= E_y^B = \hat{y} \text{ component of incident E field from B - side beam.} \end{aligned}$$

Each detector thus measures a DC term plus an interference fringe pattern modulated by the position of the dihedral mirror. Low-frequency noise will render the DC component unusable. The modulated term is proportional to the Fourier transform of the difference spectrum between one linear polarization from one input beam and the orthogonal linear polarization from the other beam.

PIXIE can operate in two modes. With the calibrator stowed, both beams view the same part of the sky. The power on each detector then becomes

$$\begin{aligned} P_{Lx} &= \frac{1}{2} \int (E_x^2 + E_y^2) + (E_x^2 - E_y^2) \cos(4z\omega/c) d\omega \\ P_{Ly} &= \frac{1}{2} \int (E_x^2 + E_y^2) - (E_x^2 - E_y^2) \cos(4z\omega/c) d\omega \\ P_{Rx} &= \frac{1}{2} \int (E_x^2 + E_y^2) + (E_x^2 - E_y^2) \cos(4z\omega/c) d\omega \\ P_{Ry} &= \frac{1}{2} \int (E_x^2 + E_y^2) - (E_x^2 - E_y^2) \cos(4z\omega/c) d\omega. \end{aligned} \quad (28)$$

We may rewrite this in terms of the Stokes parameters

$$\begin{aligned} I &= E_x^2 + E_y^2 \\ Q &= E_x^2 - E_y^2 \\ U &= 2E_x E_y \end{aligned} \quad (29)$$

to obtain

$$\begin{aligned}
P_{Lx} &= \frac{1}{2} \int I(\omega) + Q(\omega) \cos(4z\omega/c) d\omega \\
P_{Ly} &= \frac{1}{2} \int I(\omega) - Q(\omega) \cos(4z\omega/c) d\omega \\
P_{Rx} &= \frac{1}{2} \int I(\omega) + Q(\omega) \cos(4z\omega/c) d\omega \\
P_{Ry} &= \frac{1}{2} \int I(\omega) - Q(\omega) \cos(4z\omega/c) d\omega
\end{aligned} \tag{30}$$

The detected fringe pattern is thus directly proportional to the Fourier transform of the frequency spectrum of the Stokes Q linear polarization of the sky. The spacecraft spin modulates the polarized signal from the sky while leaving the unpolarized component unchanged. The sky signal

$$\vec{E} = E_x \hat{x} + E_y \hat{y} \tag{31}$$

in sky-fixed coordinates $[\hat{x}, \hat{y}]$ becomes

$$\begin{aligned}
\vec{E} &= (E_x \cos \gamma + E_y \sin \gamma) \hat{x}' \\
&+ (E_y \cos \gamma - E_x \sin \gamma) \hat{y}'
\end{aligned} \tag{32}$$

in instrument coordinates $[\hat{x}', \hat{y}']$, where γ is the spacecraft rotation angle relating the two coordinate systems. When the calibrator is in the stowed position, we may thus recover the polarization state of the sky as

$$\begin{aligned}
P_{Lx} &= \frac{1}{2} \int [Q(\omega) \cos(2\gamma) + U(\omega) \sin(2\gamma)] \cos(4z\omega/c) d\omega \\
P_{Ly} &= \frac{1}{2} \int [-Q(\omega) \cos(2\gamma) - U(\omega) \sin(2\gamma)] \cos(4z\omega/c) d\omega \\
P_{Rx} &= \frac{1}{2} \int [Q(\omega) \cos(2\gamma) + U(\omega) \sin(2\gamma)] \cos(4z\omega/c) d\omega \\
P_{Ry} &= \frac{1}{2} \int [-Q(\omega) \cos(2\gamma) - U(\omega) \sin(2\gamma)] \cos(4z\omega/c) d\omega,
\end{aligned} \tag{33}$$

where we have dropped for clarity the constant term (proportional to Stokes I) not modulated by the mirror movement.

The instrument can also operate with a blackbody calibrator blocking one aperture. Assume that the calibrator blocks the A-side beam. The detected power may now be written

$$\begin{aligned}
P_{Lx} &= \frac{1}{2} \int (E_{x,\text{sky}}^2 + E_{y,\text{cal}}^2) + (E_{x,\text{sky}}^2 - E_{y,\text{cal}}^2) \cos(4z\omega/c) d\omega \\
P_{Ly} &= \frac{1}{2} \int (E_{x,\text{cal}}^2 + E_{y,\text{sky}}^2) - (E_{x,\text{cal}}^2 - E_{y,\text{sky}}^2) \cos(4z\omega/c) d\omega \\
P_{Rx} &= \frac{1}{2} \int (E_{x,\text{cal}}^2 + E_{y,\text{sky}}^2) + (E_{x,\text{cal}}^2 - E_{y,\text{sky}}^2) \cos(4z\omega/c) d\omega \\
P_{Ry} &= \frac{1}{2} \int (E_{x,\text{sky}}^2 + E_{y,\text{cal}}^2) - (E_{x,\text{sky}}^2 - E_{y,\text{cal}}^2) \cos(4z\omega/c) d\omega
\end{aligned} \tag{34}$$

The fringe pattern now depends on the difference between the sky signal in one linear polarization and the calibrator signal in the orthogonal polarization. We may write a single linear polarization state as a linear

combination of Stokes parameters,

$$\begin{aligned} E_{x,\text{sky}}^2 &= \frac{I_{\text{sky}} + Q_{\text{sky}}}{2} \\ E_{y,\text{sky}}^2 &= \frac{I_{\text{sky}} - Q_{\text{sky}}}{2} \end{aligned} \quad (35)$$

The calibrator is unpolarized so that $\langle E_{x,\text{cal}}^2 \rangle = \langle E_{y,\text{cal}}^2 \rangle$. As the spacecraft spins, the measured fringe pattern yields the frequency spectrum of the Stokes I, Q, and U parameters from the sky,

$$\begin{aligned} P_{Lx} &= \frac{1}{4} \int [I_{\text{sky}}(\omega) - I_{\text{cal}}(\omega) + Q(\omega) \cos(2\gamma) + U(\omega) \sin(2\gamma)] \cos(4z\omega/c) d\omega \\ P_{Ly} &= \frac{1}{4} \int [I_{\text{sky}}(\omega) - I_{\text{cal}}(\omega) - Q(\omega) \cos(2\gamma) - U(\omega) \sin(2\gamma)] \cos(4z\omega/c) d\omega \\ P_{Rx} &= \frac{1}{4} \int [I_{\text{cal}}(\omega) - I_{\text{sky}}(\omega) + Q(\omega) \cos(2\gamma) + U(\omega) \sin(2\gamma)] \cos(4z\omega/c) d\omega \\ P_{Ry} &= \frac{1}{4} \int [I_{\text{cal}}(\omega) - I_{\text{sky}}(\omega) - Q(\omega) \cos(2\gamma) - U(\omega) \sin(2\gamma)] \cos(4z\omega/c) d\omega, \end{aligned} \quad (36)$$

where we again drop for clarity the constant terms (now proportional to $I_{\text{cal}} + I_{\text{sky}} + Q_{\text{sky}}$) not modulated by the mirror movement. Note the factor of two difference for the Stokes Q and U terms between Eqs. 33 and 36. When the calibrator is over one beam, the fringe pattern is sensitive to Stokes I, Q, and U. When both beams view the sky, the fringe pattern is only sensitive to linear polarization (Stokes Q and U), but at twice the signal intensity since the instrument now interferes two copies of the sky signal.

The factor of two increase in sensitivity when both beams view the sky is possible because the instrument interferes one linear polarization from one beam with the orthogonal polarization from the other beam. Circularly polarized sky emission would introduce correlations between the orthogonal linear polarization states, but continuum emission at millimeter wavelengths has no significant circular polarization.

REFERENCES

- [1] Rubakov, V. A., Sazhin, M. V., and Veryaskin, A. V., "Graviton creation in the inflationary universe and the grand unification scale," *Physics Letters B* **115**, 189–192 (Sept. 1982).
- [2] Fabbri, R. and Pollock, M. D., "The effect of primordially produced gravitons upon the anisotropy of the cosmological microwave background radiation," *Physics Letters B* **125**, 445–448 (June 1983).
- [3] Abbott, L. F. and Wise, M. B., "Constraints on generalized inflationary cosmologies," *Nuclear Physics B* **244**, 541–548 (Oct. 1984).
- [4] Polnarev, A. G., "Polarization and anisotropy induced in the microwave background by cosmological gravitational waves," *Astronomicheskii Zhurnal* **62**, 1041–1052 (Dec. 1985).
- [5] Davis, R. L., Hodges, H. M., Smoot, G. F., Steinhardt, P. J., and Turner, M. S., "Cosmic microwave background probes models of inflation," *Physical Review Letters* **69**, 1856–1859 (Sept. 1992).
- [6] Grishchuk, L. P., "Cosmological perturbations of quantum-mechanical origin and anisotropy of the microwave background," *Physical Review Letters* **70**, 2371–2374 (Apr. 1993).
- [7] Kamionkowski, M., Kosowsky, A., and Stebbins, A., "Statistics of cosmic microwave background polarization," *Physical Review D* **55**, 7368–7388 (June 1997).
- [8] Seljak, U. and Zaldarriaga, M., "Signature of Gravity Waves in the Polarization of the Microwave Background," *Physical Review Letters* **78**, 2054–2057 (Mar. 1997).
- [9] Turner, M. S. and White, M., "Dependence of inflationary reconstruction upon cosmological parameters," *Physical Review D* **53**, 6822–6828 (June 1996).

- [10] Komatsu, E., Dunkley, J., Nolta, M. R., Bennett, C. L., Gold, B., Hinshaw, G., Jarosik, N., Larson, D., Limon, M., Page, L., Spergel, D. N., Halpern, M., Hill, R. S., Kogut, A., Meyer, S. S., Tucker, G. S., Weiland, J. L., Wollack, E., and Wright, E. L., “Five-Year Wilkinson Microwave Anisotropy Probe Observations: Cosmological Interpretation,” *Astrophysical Journal Supplement Series* **180**, 330–376 (Feb. 2009).
- [11] Bock, J., Church, S., Devlin, M., Hinshaw, G., Lange, A., Lee, A., Page, L., Partridge, B., Ruhl, J., Tegmark, M., Timbie, P., Weiss, R., Winstein, B., and Zaldarriaga, M., “Task Force on Cosmic Microwave Background Research,” *ArXiv Astrophysics e-prints* (Apr. 2006).
- [12] Dunkley, J., Amblard, A., Baccigalupi, C., Betoule, M., Chuss, D., Cooray, A., Delabrouille, J., Dickinson, C., Dobler, G., Dotson, J., Eriksen, H. K., Finkbeiner, D., Fixsen, D., Fosalba, P., Fraisse, A., Hirata, C., Kogut, A., Kristiansen, J., Lawrence, C., Magalhães, A. M., Miville-Deschenes, M. A., Meyer, S., Miller, A., Naess, S. K., Page, L., Peiris, H. V., Phillips, N., Pierpaoli, E., Rocha, G., Vaillancourt, J. E., and Verde, L., “Prospects for polarized foreground removal,” in [*American Institute of Physics Conference Series*], S. Dodelson, D. Baumann, A. Cooray, J. Dunkley, A. Fraisse, M. G. Jackson, A. Kogut, L. Krauss, M. Zaldarriaga, & K. Smith, ed., *American Institute of Physics Conference Series* **1141**, 222–264 (June 2009).
- [13] Dodelson, S., et al., “The Origin of the Universe as Revealed Through the Polarization of the Cosmic Microwave Background,” in [*astro2010: The Astronomy and Astrophysics Decadal Survey*], *Astronomy* **2010**, 67+ (2009).
- [14] Wollack, E. J., Fixsen, D. J., Henry, R., Kogut, A., Limon, M., and Mirel, P., “Electromagnetic and Thermal Properties of a Conductively Loaded Epoxy,” *International Journal of Infrared and Millimeter Waves* **29**, 51–61 (Jan. 2008).
- [15] Mather, J. C., “The Cosmic Background Explorer /COBE/,” *Optical Engineering* **21**, 769–774 (Aug. 1982).
- [16] Kogut, A., Fixsen, D. J., Chuss, D. T., Dotson, J., Dwek, E., Halpern, M., Hinshaw, G. F., Meyer, S. M., Moseley, S. H., Seiffert, M. D., Spergel, D. N., and Wollack, E. J., “The Primordial Inflation Explorer (PIXIE): a nulling polarimeter for cosmic microwave background observations,” *Journal of Cosmology and Astroparticle Physics* **7**, 25+ (July 2011).
- [17] Fraisse, A. A., Brown, J. C., Dobler, G., Dotson, J. L., Draine, B. T., Frisch, P. C., Haverkorn, M., Hirata, C. M., Jansson, R., Lazarian, A., Magalhães, A. M., Waelkens, A., and Wolleben, M., “CMBPol Mission Concept Study: Foreground Science Knowledge and Prospects,” *ArXiv e-prints* (Nov. 2008).
- [18] Bennett, C. L., Smoot, G. F., Hinshaw, G., Wright, E. L., Kogut, A., de Amici, G., Meyer, S. S., Weiss, R., Wilkinson, D. T., Gulkis, S., Janssen, M., Boggess, N. W., Cheng, E. S., Hauser, M. G., Kelsall, T., Mather, J. C., Moseley, Jr., S. H., Murdock, T. L., and Silverberg, R. F., “Preliminary separation of galactic and cosmic microwave emission for the COBE Differential Microwave Radiometer,” *The Astrophysical Journal Letters* **396**, L7–L12 (Sept. 1992).
- [19] Bennett, C. L., Hill, R. S., Hinshaw, G., Nolta, M. R., Odegard, N., Page, L., Spergel, D. N., Weiland, J. L., Wright, E. L., Halpern, M., Jarosik, N., Kogut, A., Limon, M., Meyer, S. S., Tucker, G. S., and Wollack, E., “First-Year Wilkinson Microwave Anisotropy Probe (WMAP) Observations: Foreground Emission,” *The Astrophysical Journal Supplement Series* **148**, 97–117 (Sept. 2003).
- [20] Finkbeiner, D. P., Davis, M., and Schlegel, D. J., “Extrapolation of Galactic Dust Emission at 100 Microns to Cosmic Microwave Background Radiation Frequencies Using FIRAS,” *The Astrophysical Journal* **524**, 867–886 (Oct. 1999).
- [21] Hildebrand, R. and Kirby, L., “Polarization of FIR/Sub-mm Dust Emission,” in [*Astrophysics of Dust*], A. N. Witt, G. C. Clayton, & B. T. Draine, ed., *Astronomical Society of the Pacific Conference Series* **309**, 515+ (May 2004).
- [22] Hu, W., Hedman, M. M., and Zaldarriaga, M., “Benchmark parameters for CMB polarization experiments,” *Physical Review D* **67**, 043004+ (Feb. 2003).
- [23] Carretti, E., Cortiglioni, S., Sbarra, C., and Tascone, R., “Antenna instrumental polarization and its effects on E- and B-modes for CMBP observations,” *Astronomy & Astrophysics* **420**, 437–445 (June 2004).
- [24] Shimon, M., Keating, B., Ponthieu, N., and Hivon, E., “CMB polarization systematics due to beam asymmetry: Impact on inflationary science,” *Physical Review D* **77**, 083003+ (Apr. 2008).

- [25] MacTavish, C. J., Ade, P. A. R., Battistelli, E. S., Benton, S., Bihary, R., Bock, J. J., Bond, J. R., Brevik, J., Bryan, S., Contaldi, C. R., Crill, B. P., Doré, O., Fissel, L., Golwala, S. R., Halpern, M., Hilton, G., Holmes, W., Hristov, V. V., Irwin, K., Jones, W. C., Kuo, C. L., Lange, A. E., Lawrie, C., Martin, T. G., Mason, P., Montroy, T. E., Netterfield, C. B., Riley, D., Ruhl, J. E., Runyan, M., Trangsrud, A., Tucker, C., Turner, A., Viero, M., and Wiebe, D., “Spider Optimization: Probing the Systematics of a Large-Scale B-Mode Experiment,” *The Astrophysical Journal* **689**, 655–665 (Dec. 2008).
- [26] Brown, M. L., Challinor, A., North, C. E., Johnson, B. R., O’Dea, D., and Sutton, D., “Impact of modulation on CMB B-mode polarization experiments,” *Monthly Notices of the Royal Astronomical Society* **397**, 634–656 (Aug. 2009).
- [27] Miller, N. J., Shimon, M., and Keating, B. G., “CMB polarization systematics due to beam asymmetry: Impact on cosmological birefringence,” *Physical Review D* **79**, 103002–+ (May 2009).
- [28] Takahashi, Y. D., Ade, P. A. R., Barkats, D., Battle, J. O., Bierman, E. M., Bock, J. J., Chiang, H. C., Dowell, C. D., Duband, L., Hivon, E. F., Holzapfel, W. L., Hristov, V. V., Jones, W. C., Keating, B. G., Kovac, J. M., Kuo, C. L., Lange, A. E., Leitch, E. M., Mason, P. V., Matsumura, T., Nguyen, H. T., Ponthieu, N., Pryke, C., Richter, S., Rocha, G., and Yoon, K. W., “Characterization of the BICEP Telescope for High-precision Cosmic Microwave Background Polarimetry,” *The Astrophysical Journal* **711**, 1141–1156 (Mar. 2010).
- [29] Bock, J., Aljabri, A., Amblard, A., Baumann, D., Betoule, M., Chui, T., Colombo, L., Cooray, A., Crumb, D., Day, P., Dickinson, C., Dowell, D., Dragovan, M., Golwala, S., Gorski, K., Hanany, S., Holmes, W., Irwin, K., Johnson, B., Keating, B., Kuo, C.-L., Lee, A., Lange, A., Lawrence, C., Meyer, S., Miller, N., Nguyen, H., Pierpaoli, E., Ponthieu, N., Puget, J.-L., Raab, J., Richards, P., Satter, C., Seiffert, M., Shimon, M., Tran, H., Williams, B., and Zmuidzinas, J., “Study of the Experimental Probe of Inflationary Cosmology (EPIC)-Intermediate Mission for NASA’s Einstein Inflation Probe,” *ArXiv e-prints* (June 2009).
- [30] O’Dea, D. T., Ade, P. A. R., Amiri, M., Benton, S. J., Bock, J. J., Bond, J. R., Bonetti, J. A., Bryan, S., Burger, B., Chiang, H. C., Clark, C. N., Contaldi, C. R., Crill, B. P., Davis, G., Dore, O., Farhang, M., Filippini, J. P., Fissel, L. M., Fraisse, A. A., Gandilo, N. N., Golwala, S., Gudmundsson, J. E., Hasselfield, M., Hilton, G., Holmes, W., Hristov, V. V., Irwin, K., Jones, W. C., Kuo, C. L., MacTavish, C. J., Mason, P. V., Montroy, T. E., Morford, T. A., Netterfield, C. B., Rahlin, A. S., Reintsema, C., Ruhl, J. E., Runyan, M. C., Schenker, M. A., Shariff, J. A., Soler, J. D., Trangsrud, A., Tucker, C., Tucker, R. S., Turner, A. D., and Wiebe, D., “Spider Optimization II: Optical, Magnetic and Foreground Effects,” *ArXiv e-prints* (Feb. 2011).